Light-controlled micromotors and soft microrobots

Stefano Palagi, Dhruv P. Singh, and Peer Fischer*

Dr. S. Palagi
Center for Micro-BioRobotics, Istituto Italiano di Tecnologia
viale R. Piaggio 34, 56025 Pontedera (PI), Italy, and
Micro, Nano, and Molecular Systems, Max Planck Institute for Intelligent Systems
Heisenbergstr. 3, 70569 Stuttgart, Germany
E-Mail: stefano.palagi@iit.it

Dr. D. P. Singh
Department of Physics, Indian Institute of Technology Bhilai
GEC Campus, Sejbahar, Raipur, Chhattisgarh 492015, India, and
Micro, Nano, and Molecular Systems, Max Planck Institute for Intelligent Systems
Heisenbergstr. 3, 70569 Stuttgart, Germany

Prof. Dr. P. Fischer
Micro, Nano, and Molecular Systems, Max Planck Institute for Intelligent Systems
Heisenbergstr. 3, 70569 Stuttgart, Germany, and
Institute of Physical Chemistry, University of Stuttgart
Pfaffenwaldring 55, 70569 Stuttgart, Germany

Keywords: micromotors, soft microrobots, light-based control, photoresponsive materials

Mobile microscale devices and microrobots can be powered by catalytic reactions (chemical micromotors) or by external fields. In this report, we focus on the role of light as a versatile means for wirelessly powering and controlling such microdevices. Recent advances in the development of autonomous micromotors are discussed, where light permits their actuation with unprecedented control and thereby enables advances in the field of active matter. In addition, structuring the light field is a new means to drive soft microrobots that are based on (photo-) responsive polymers. The behavior of the two main classes of thermo- and photo-responsive polymers adopted in microrobotics (PNIPAM and liquid-crystal elastomers) is analyzed, and recent applications are reported. The advantages and limitations of controlling micromotors and microrobots by light are reviewed, and some of the remaining challenges in the development of novel photo-active materials for micromotors and microrobots are discussed.

1. Introduction

Light is extremely versatile as it can be used to transmit both energy and information. Life on earth is powered by sunlight, and we use light in the fabrication of integrated circuits, in high bandwidth communication, material processing, to detect single molecules, and for laser-assisted surgery. Indeed, modern consumer products, manufacturing, quality control and research in many scientific fields are directly impacted by light, and lasers in particular. Light as an electromagnetic wave can show exquisite spatial and temporal control. In contrast, magnetic and electric fields alone cannot be easily focused or structured in space. Similarly, acoustic fields cannot match the resolution achievable with light. It is therefore no surprise that light is also used to drive and control artificial machinery and structures at the micro and nanoscale. Light has shown its potential in powering and actuating devices in optically accessible media, but suffers from a limitation when it comes to applications in opaque media, including, for instance, deep inside the human body.

The most direct form of manipulating objects with light is to use a focused light beam to trap and hold objects [1]. Such an 'optical tweezer' can exert forces on micro-devices, and has been successfully used to operate microrobots consisting of microfabricated microstructures [2]. Although very powerful and widely adopted for a variety of applications, optical tweezers can only manipulate micron-size objects at close range and require high local light intensities. Alternatively, light can also be used to control and/or power microscopic particles and devices at a distance, especially when the material interacts favorably with light, as we discuss here.

In this Progress Report we highlight some recent advances in manipulating photoresponsive microstructures in liquid environments. Such photo-active systems show complex behaviors due to the interplay of the light field with the material and can be used to develop light-

controlled clocks, motors, microswimmers and nanomachines using only very simple building blocks.

2. Light-controlled micromotors (LMMs)

In its simplest form, even a spherical particle can be a micromotor that can self-propel in a fluid medium. If the particle has two dissimilar halves, known as a "Janus" particle [3,4] having a light-active and an inactive surface on opposite sides, light can trigger a local reaction via a photo-catalytic process or partial heating of the active surface of the colloid. This breaks the local symmetry of the colloid and local fluid flows result in response, which in turn cause the propulsion of the particle (see Fig. 1 for a schematic) [5,6] – not because the light field exerts a force, but because the light field facilitates a chemical reaction or provides energy for these simplest motors. Light-powered colloidal motors show a rich phenomenology and can be designed to move independently in random directions, or respond to external fields and cues. These light-enabled "microswimmers" depend on light, like many organisms, but unlike their biological counterparts their swimming is due to the physics and chemistry near their surface which does not require any biochemical processes. Artificial self-propelled motors nevertheless show a fascinating phenomenology that one normally associates with the living world and are therefore important model systems to study "active" and "non-equilibrium phenomena".

There are further approaches to design light-driven micromotors by for instance using bubble based propulsion or by inducing temperature gradients to drive thermophoretic swimmers [7–11]. A detailed discussion regarding the designs for light-controlled micromotors has been provided in previous reviews [12–14]. In this report, we focus on chemical micromotors that move in a fluid by light-induced self-diffusiophoresis and present the most recent improvements in the design of these micromotors. These chemically-active microswimmers constitute a class of micromotors where the light intensity or wavelength can be used to control the rate of a chemical reaction. Light can thus be used to control as well as turn the micromotors' movement

on or off. These swimmers can be used to study the emergence of collective behaviors and to quantify the role of activity in self-assembly processes, and be used for reconfigurable materials, cargo delivery systems, or to tune material properties with light.

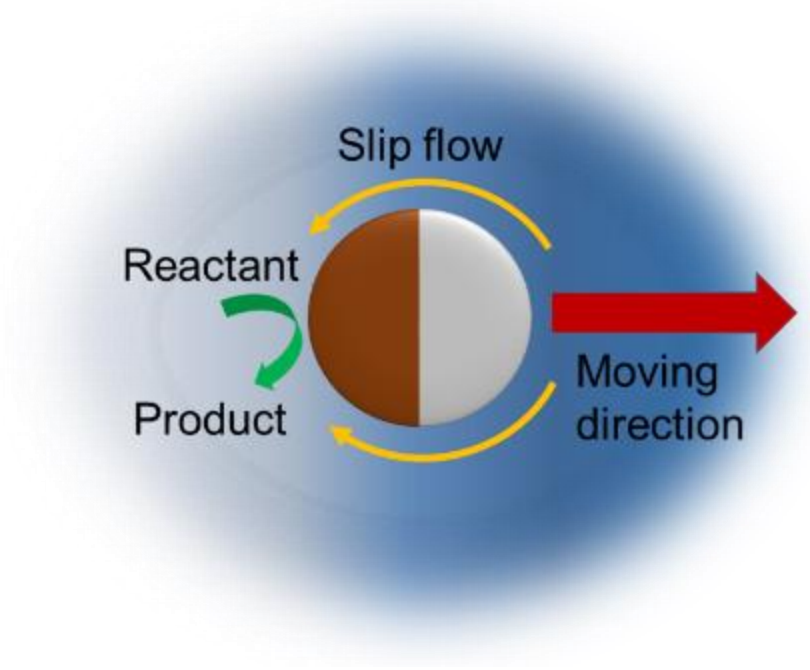

Figure 1. Schematic of catalytic propulsion of a catalytic Janus micromotor

In addition to light-induced swimming, photo-active micromotors can also sense the gradient in the intensity of the incident light and thus become *phototactic*. This feature provides a novel way to control the movement of the micromotors. In recent years, the fabrication of light controlled micromotors has progressed and in particular it has been possible to reduce the required light intensity for propulsion and to observe self-propulsion in different liquids. We will first briefly discuss design strategies and the material selection and then we will discuss some examples of light-directed control of micromotors. After a discussion of the light-controlled micromotors, we will consider photo-active polymeric microrobots.

2.1. Materials selection for micromotors

The primary criteria to choose photo-chemically active materials for light-controlled micromotors is their spectral response and their photo-catalytic activity. Wide band gap

semiconductor materials, that have high photocatalytic efficiency like titanium dioxide (TiO_2) and hematite (Fe_2O_3) are attractive and have been used in the first generation of chemically-powered LMMs. Upon excitation by light, electron-hole pairs are formed that can participate in chemical reactions in solution. The efficiency of the reaction depends on the relative position of the energy levels of the chemicals and the valance- and conduction-bands of the semiconductor. Hydrogen peroxide is a high-energy chemical (it is used as rocket fuel) that has been used to power many microswimmers [15–19], and it has also been used as a fuel for many light-controlled micromotors [20]. Janus spheres [21] (Fig. 2(a)) and rods, as well as inert spheres with the protruding catalyst [22,23] (Fig. 2b), asymmetric particles [24,25] (Fig. 2(c)), and dynamic colloidal clusters [26] have all been successfully activated by light in aqueous hydrogen peroxide solutions.

Apart from using semiconductors for light-driven catalytic reactions, it has also been shown that light-powered micromotors can swim by inducing phase separation of a binary mixture near the critical point [27,28]. Buttinoni *et al*. used Janus particles with a half-coating of a light-absorber (carbon or gold); when immersed in a *water-lutidine* solution, a small temperature increase near the absorbing surface causes de-mixing of the solution, which in turn induces local flows and self-propulsion due to self-diffusiophoresis (see Fig. 2(d)). The advantage of this system is that it does not consume the fuel, so that it can run for a long time, and that complex behaviors involving large numbers of colloids can be observed, which can also be modeled theoretically [29–32]. This colloidal system is a powerful tool for fundamental studies. However, the binary mixture has to be carefully prepared and is only effective in a very small temperature range. In all of these micromotors, including the semiconductor-based ones, good propulsion behavior has been observed with average speeds of up to 6 body lengths per second.

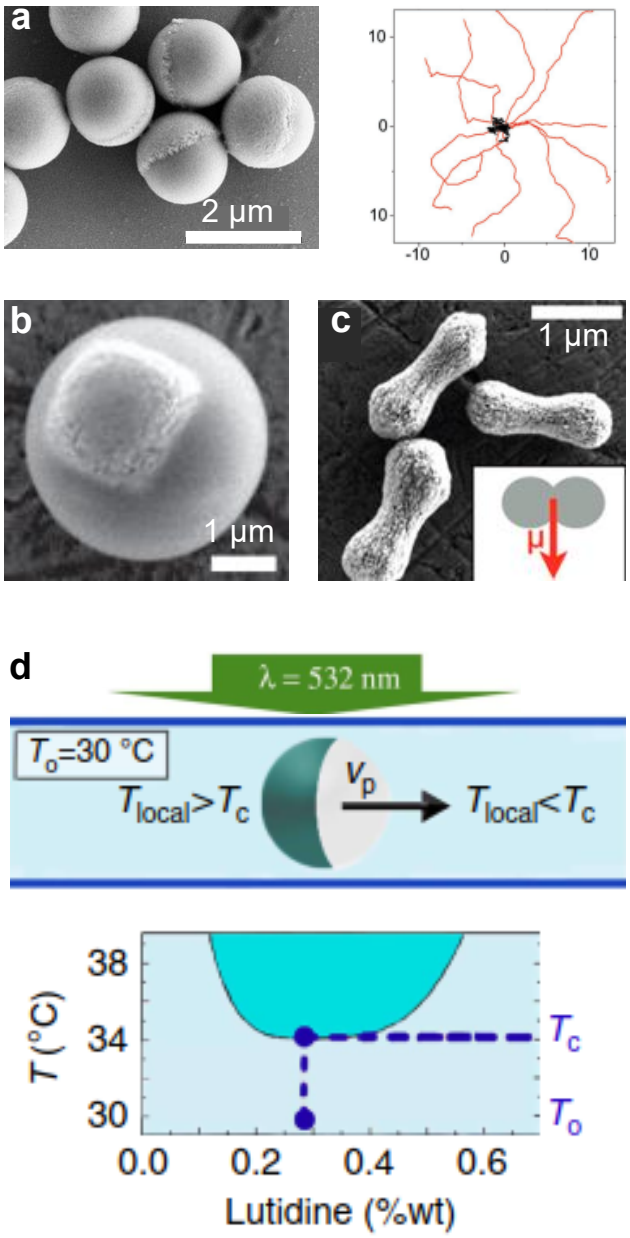

Figure 2. Light-controlled Micromotors. (a) SEM image of TiO_2-SiO_2 Janus micromotors with a TiO_2 cap on a SiO_2 sphere. Right: Trajectories of active Janus particles when the UV light is on (red) and off (black) over 3 s. The units in the panel are μm. (Adapted with permission.[21] Copyright 2017, WILEY-VCH Verlag GmbH & Co. KGaA, Weinheim). (b) SEM polymer colloidal sphere with protruding hematite cube (dark). (Adapted with permission.[22] Copyright 2014, The Author(s) Published by the Royal Society). (c) SEM picture of the shape asymmetric hematite peanut particles. Inset shows the direction of the permanent magnetic moment μ of the particle, perpendicular to the long axis. The magnetic moment can be used to control the micromotors externally. (Adapted with permission.[24] Copyright 2013, American Chemical Society). (d) Top: Schematic representation of the self-propulsion of Janus micromotor by light in binary mixture for water-lutidine. Bottom: Phase diagram of the binary mixture of 2,6-lutidine and water. (Adapted under the terms of the CC BY license.[33] Copyright 2016, The Author(s)).

The use of UV or near UV light for the excitation of micromotors, the use of hydrogen peroxide, or the carefully tuned binary solutions are all drawbacks when it comes to applications,

especially in biological media. This motivated researchers to design alternative light-controlled micromotors that can move in more biocompatible solutions. Dong *et al*. showed that, by replacing the inert oxide surface of the catalytic Janus particles by gold (Au), Au-TiO_2 Janus particles can swim in water without the need for hydrogen peroxide [34]. The presence of gold facilitates the separation of generated charge pairs as electrons move from the conduction band of the TiO_2 to the gold surface. The charge separation reduces the recombination rate of electrons and holes that take part in the chemical reaction and hence increases the overall reaction rate. Under UV-light TiO_2 can decompose pure water, however, the decomposition rate is typically very low and not useful to drive micromotors. However, the enhanced charge separation in the Au-TiO_2 structures permits the micromotors to swim in pure water with a speed of up to 25 body lengths per second, which is a significant speed at the microscale. Figure 3(a) shows the schematic of the micromotor propulsion and the observed trajectories in pure water. Similar observation of propulsion in pure water based on the charge separation mechanism under UV light illumination was also made for Au-WO_3/C (C (carbon)-WO_3 (tungsten trioxide) composite), Cu-TiO_2, and TiO_2-Pt Janus micromotors [35–37].

The requirement for UV excitation can be removed by selecting semiconductors with a more suitable bandgap, or by sensitizing wide band-gap semiconductors such that they are active at visible and infrared wavelengths. Copper oxide (Cu_2O), bismuth iodide oxide (BiOI), and black-TiO_2 (B-TiO_2) are shown as promising materials that can be triggered by visible light [38–40]. For BiOI and Au-black/TiO_2 materials propulsion in pure water could be shown [39,40]. Interestingly, the spectral response of the visible light driven micromotors is such that a number of wavelengths can be used to power them (see Fig. 3(b) and 3(c)). For certain applications it is useful to use particular wavelengths for selective excitation of individual structures, as well as to address specific micromotors. Zheng *et al*. showed that micromotors that possess a distinct spectral response, because they were sensitized with a specific dye, respond only to light in a

selected wavelength range [41]. The design of such micromotors and their wavelength selective swimming activity is shown in Fig. 3(d).

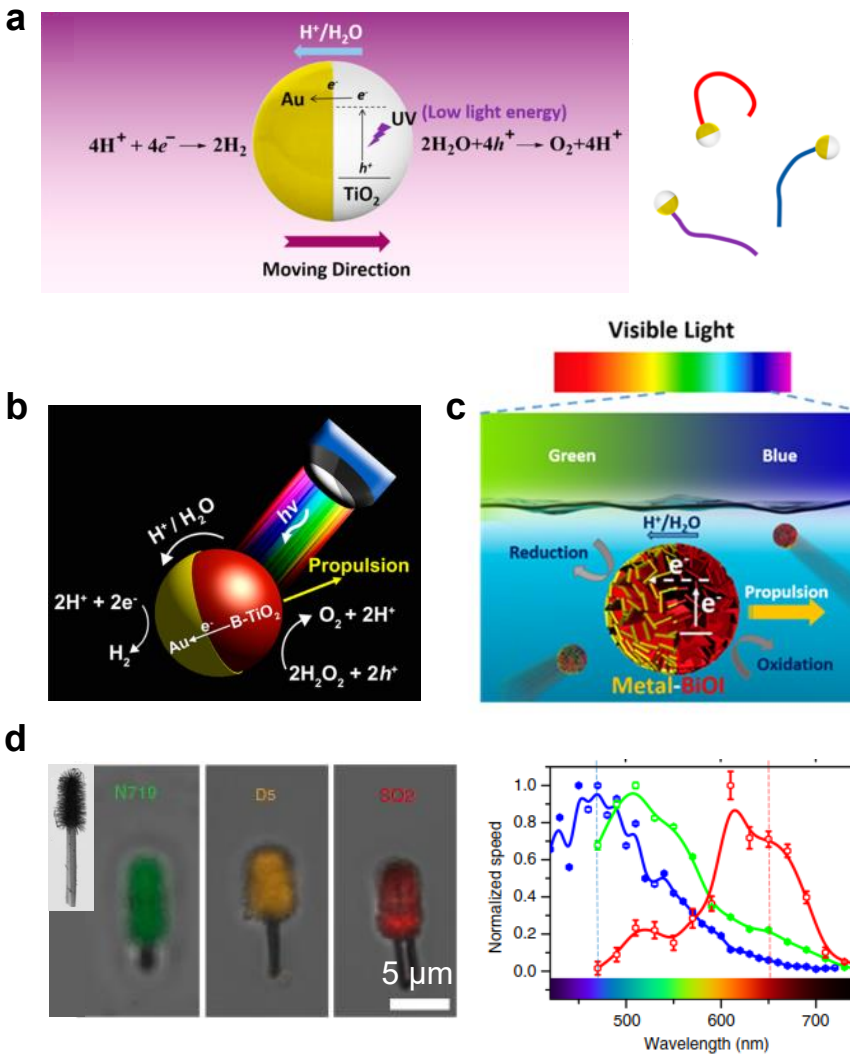

Figure 3. Hybrid LMMs. (a) Schematic of the design and propulsion mechanism of TiO_2–Au Janus micromotors, Right: trajectories of the micromotors in pure water. (Adapted with permission.[34] Copyright 2015, American Chemical Society). (b) schematic of full visible light (>400 nm) driven Au/B-TiO_2 Janus micromotors. (Reproduced with permission.[40] Copyright 2017, American Chemical Society). (c) Schematic of visible-light-driven BiOI-metal Janus micromotors. (Reproduced with permission.[39] Copyright 2017, American Chemical Society). Dye-sensitized micromotors, (d) Confocal fluorescence images of dye-sensitized microswimmers, which show that all three dyes are selectively loaded onto the TiO_2 nanowire surface, the inset shows the SEM image of the micromotor before loading the dye, Right: The normalized speed of dye-sensitized micromotors (D5 (blue), N719 (green) and SQ2 (red)). (Adapted under the terms of the CC BY license.[41] Copyright 2017, The Author(s)).

2.1.1. Material combinations for improved activity

Combining several catalytic materials can also improve the activity and swimming behavior of the micromotors. Judy *et al.* fabricated TiO_2 and Cu_2O hybrid micromotors [42], which presented wavelength-dependent modes of motion (translation or rotation) due to the different

response of the respective photocatalysts (see Fig. 4(a)). In general, the nature of the locomotion depends on the exact shape (geometry) of the micromotors, which cannot easily be changed. It is therefore attractive to find possibilities to change the swimming mode simply by changing the wavelength of the light-excitation.

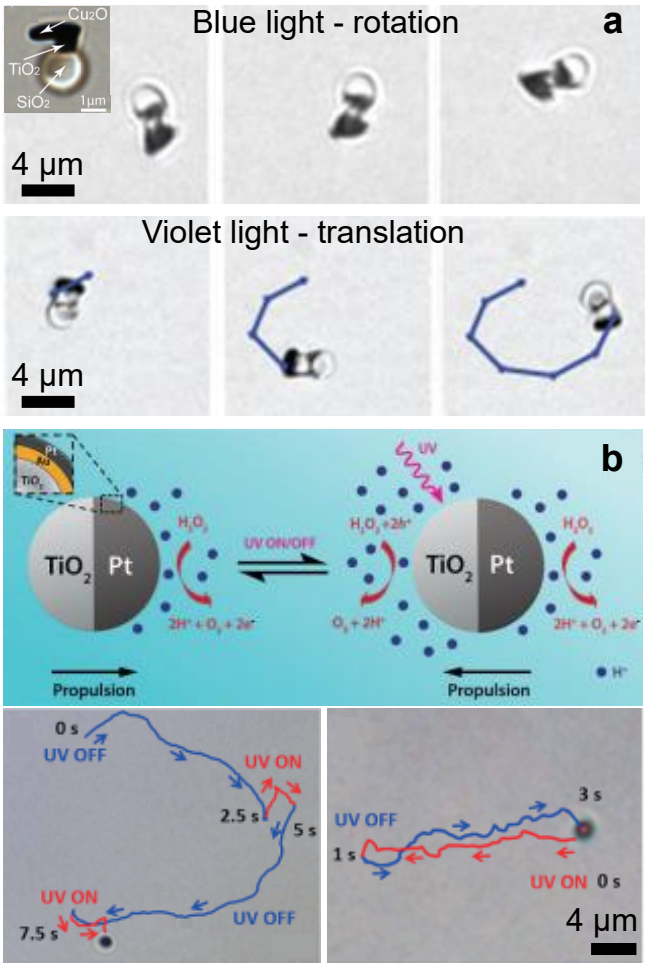

Figure 4. Hybrid LMMs for improved activity. (a) Series of video frames showing the rotation and translation motion of micromotor under blue and violet illumination, respectively. Inset shows a high-resolution micrograph of a Cu_2O- TiO_2 hybrid micromotor with labels showing the location of each material. (Adapted with permission.[42] Copyright 2018, WILEY-VCH Verlag GmbH & Co. KGaA, Weinheim). (b) Schematic of propulsion of TiO_2-Au/Pt Janus micromotor with and without illumination. Bottom left: "On-the-fly" optical brake. Bottom left: Reverse motion of micromotor propelled initially under the light-driven mode (0–1 s, red trajectory); turning the UV light off reverses the direction of the moving Janus micromotor (1–3 s, blue trajectory). (Adapted with permission.[43] Copyright 2018, WILEY-VCH Verlag GmbH & Co. KGaA, Weinheim).

An alternative scheme to add control is to add a light-controlled "brake" to an ordinary chemically-powered micromotor. Chen *at al*. demonstrated this by combining a catalytic platinum-coating with a photocatalytic (TiO_2) material [43]. In an aqueous H_2O_2 solution, the Pt-

surface is always active and drives the motion of the micromotors. However, light can switch on the TiO_2-end of the particle, which induces motion in the opposite direction and thus acts as an optical break. In the case of strong photocatalytic activity this even causes a reversal of the swimming direction (see Fig. 4(b) for the micromotor design and swimming behavior). The adaptive dual operation of such hybrid micromotors holds considerable promise for designing smart micro-machines that autonomously reconfigure their propulsion mode for various on-demand operations.

2.2. Light guided propulsion of LMMs

Some microorganisms can respond to light such that they re-orient and swim towards or away from the light source, which is known as *phototaxis*. Artificial micromotors that show phototactic behaviors will allow their orientation and positioning simply by changing the illumination conditions. Phototactic responses have recently been demonstrated in light controlled micromotors. Chen *et al*. presented a simple design of phototactic micromotors [44]. They used isotropic particles made of a single semiconducting materials (TiO_2, ZnO, or CdS) and illuminated them with light from a particular direction. Since the light is absorbed in the material, only the side of the particle that faces the light will be photocatalytically active. This inhomogenous illumination of the isotropic particles effectively turns them into a Janus like micromotor having a chemically active and an inactive surface. These isotropic (but anisotropically illuminated) micromotors move along the direction of incident light (see Fig. 5(a)). Further, since the moving direction of a Janus micromotor depends on the direction of the fluid flows along its surface, both positive and negative phototaxis i.e. the movement towards or away from the light source can be observed, depending on the material of the micromotors. Dai *et el*. showed that Janus (Si-TiO_2) nanotree like swimmers (design as in Fig. 3(d)) have the ability to respond to the illumination (365 nm) direction and align their body axes parallel to that direction [25]. Interestingly, the movement of swimmers along the light

direction can be programmed to show positive or negative phototaxis by adding chemicals that control the formation of the reaction products or that change the zeta potential of the particle's surface (see Fig. 5(b)). These studies demonstrate that photo-active reactions can be used to finely control the moving trajectory of the micromotors without having to directly exert forces on the particles. Figure 5(b) bottom, shows the trajectory of such a Janus nanotree spelling the word 'nano'.

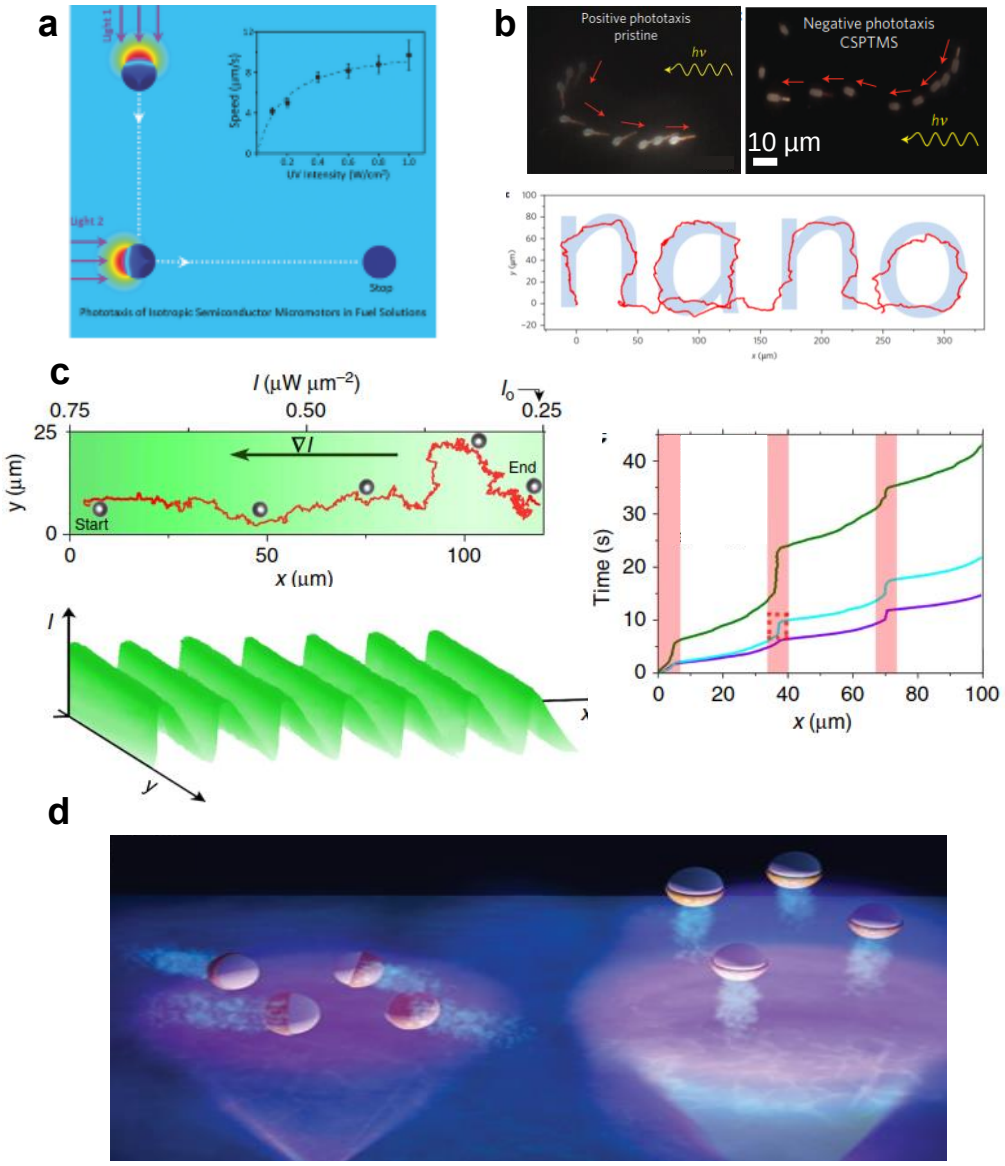

Figure 5. Light guided propulsion of LMMs. (a) Phototactic motion of isotropic micromotor along the light path. (Reproduced with permission.[44] Copyright 2016, WILEY-VCH Verlag GmbH & Co. KGaA, Weinheim). (b) Programmable phototaxis (positive or negative) of an individual Janus micromotor by chemical treatment. The bottom figure shows the trajectory of a micromotor that writes 'nano', navigated by light. (Adapted with permission.[25] Copyright 2016, Macmillan Publishers Limited, part of Springer Nature). (c) Phototactic particle motion in constant light gradients. Bottom: the saw tooth wave light profile to obtain directed motion over longer

distances. Right: the trajectories of a micromotor across the saw tooth profile, pink and white region represent the regions of increasing and decreasing intensity, respectively. Different color of tracks are for different intensity gradients. Maximum gradient (purple) leads to the fastest track. (Adapted under the terms of the CC BY license.[33] Copyright 2016, The Author(s)). (d) Controlled in-plane and out of plane swimming. Schematic showing the in-plane (2D) and out of plane (3D) swimming at low and high light intensities respectively (Reproduced with permission.[45] Copyright 2018, WILEY-VCH Verlag GmbH & Co. KGaA, Weinheim).

In both these examples, the observation of phototactic swimming demands the incidence of light parallel to the swimming plane (X-Y plane): A change of the swimming requires that the position of the light source is altered, or that several different light sources are operated. A potentially simpler way to control the motion was demonstrated by Lozano *et al*., who showed that the motion of micromotors could be controlled with a single light source [33]. Working with Janus (carbon-SiO_2) particles in a binary water-lutidine mixture (see Fig. 2(d)) they observed that when they projected light with a linear in-plane intensity gradient, the particles align such that they move along the gradient towards low light intensities (see Fig. 5(c)). Such directional movement requires a strong gradient as well as high light intensity, which can be maintained only within a narrow region. Therefore, with a single intensity pattern, the micromotors can be directed only over a small distance. A saw-tooth shaped static light profile repeats the intensity gradient and thus rectifies the motion of the particles over longer distances. The intensity profile in the saw-tooth pattern had a narrow region where the intensity increases, such that the particles move relatively quickly through this region and on average do not re-orient much (transit times are on average shorter than the rotational diffusion time). Therefore, when the micromotor reaches the increasing light intensity, it passes to the next region of decreasing light intensity without reversing its direction of motion. A track of a micromotor through a saw-tooth intensity pattern is shown in Fig. 5(c). The technique provides an elegant and surprising means to direct the motion of micromotors in a plane with a single static light source.

Most of the studies so far have been limited to motion in two dimensions. However, Singh *et al.* showed the possibility of controlling the motion of micromotors in three dimensions [45]. Janus micromotors (TiO_2-SiO_2) illuminated with low intensity light normally swim along the

bottom of a container, where they have sedimented. However, they can re-orient when illuminated with light of a sufficiently high intensity, such that they lift off from the surface and swim upwards against gravity in a 3D trajectory away from the light source. Figure 5(d) shows different states of the motion of such micromotors. This study provides a simple design strategy to fabricate artificial micromotors whose two- or three- dimensional swimming behavior can be controlled with light.

3. Light-controlled soft microrobots

As mentioned above, light is emerging as a means for controlling not only micromotors but also microrobots. These are untethered, mobile robotic devices with sizes in the submillimeter range (micron to millimeter) [46]. Potential envisioned applications of microrobots are minimally-invasive or non-invasive medical procedures (such as in endoscopy or for targeted delivery of drugs and cells)[47], lab-on-a-chip applications, and microfabrication.

The term 'robot' refers to mechanical machines that can be controlled or programmed to execute specific tasks, ideally autonomously. Robots usually contain electromechanical components, such as motors and actuators, sensors, controllers, batteries, that allow them to move, interact with their environment, and execute their tasks. However, miniaturizing these components to the microscale, assembling and integrating them in submillimeter-size mobile robotic devices is currently not feasible. For this reason, 'microrobots' often consist of micro- or nanofabricated structures with no on-board sensing, actuation, or control, but which are usually moved and wirelessly controlled by external fields, such as magnetic fields [48] or, more recently, light. Strictly, field-controlled micro- and nanorobots are really robotic *systems* that contain macro-scale control elements.

Magnetic fields and gradients are a preferred means for controlling and actuating micro- and nanorobots including magnetic materials, as they can wirelessly exert torques and forces, respectively. For instance, quasi-static magnetic fields and gradients can be used to orient and

'pull' simple magnetic micro-objects [49,50]. Alternatively, microrobots can be fabricated that consist of a magnetic *head* and a *tail*, or propeller. Microrobots with a rigid helical propeller are actuated by a rotating magnetic field, which exerts a torque on the magnetic head and results in continuous rotation and propulsion of the microrobot in a liquid [51,52]. For microrobots with a flexible slender propeller, either a rotating field is applied, also resulting in helical propulsion, or an oscillating field is used to induce propulsive beating of the flexible tail in the liquid [53]. Magnetic fields, however, cannot be finely modulated in space, which makes independently controlling more than one microrobot in parallel (or, especially, different parts of the same microrobot) very challenging.

In comparison, light is a promising and versatile means for achieving fine and selective control of microrobots. Optical fields can exert small forces on microscale objects that are sufficient to cause movement in a controlled way. For instance, micron-size particles can be trapped, held, and moved by highly focused light beams, known as optical tweezers [1], depending on the refractive index of the particle with respect to that of the surrounding medium. Exerting optical forces and torques on micro- and nano-structures, light-actuated micro-tools and microrobots have been developed [54]. For instance, optical microrobotics tools have been presented that are moved and controlled by multiple dual-beam optical traps and also have a light-controlled, convection-based syringe function [55].

Recently, much progress has been made to make microrobots out of soft and *smart* materials [56] – an approach referred to as *soft microrobotics*. For instance, magnetic soft microrobots have been presented that consist of magnetic nanoparticles-laden hydrogels which can float in water, resulting in more effective actuation and simpler control [50,57,58]. Even more advantageous is the use of soft materials that respond to external stimuli with mechanical deformations: these can be used to provide microscale robots with actual robotic functionalities, such as on-board sensing and actuation [59], improving their performance [60] and leading to

microrobots with increased adaptability and flexibility [56]. Among stimuli-responsive materials, smart polymers that mechanically respond to temperature changes (thermoresponsive) or to light (photoresponsive) have allowed microrobots to excise cells [61], release drugs [62], or reconfigure their shape [63,64].

Compared to magnetic- and light-actuated microrobots and micro-tools, where the magnetic and light field actually exert forces and/or torques on the microrobots' body, in soft photoresponsive microrobots the light field *only* powers and controls the actuation wirelessly. In other words, light-controlled soft microrobots have the intrinsic ability to generate forces on their environment by means of their photoresponsive material body.

3.1. Photoresponsive materials for microrobots

Polymeric materials, elastomers, and hydrogels that respond to light with a mechanical deformation can be used as remotely controlled on-board actuators for microrobots. These materials are often based on thermoresponsive materials that include photo-absorbing particles or molecules. Whereas it is possible to directly exploit the thermal response of the materials [65] or to induce it by inductive heating of embedded magnetic particles [66], triggering the response by light represents the most practical and versatile approach. Light-induced heating at the microscale can indeed be particularly effective and elicit a fast response [67]. Moreover, the cooling phase, which often represents the limiting step in using thermoresponsive materials, is also quite fast at the microscale, resulting in potentially high actuation frequencies [68].

The most common photoresponsive materials for soft microrobots are hydrogels based on lower critical solution temperature polymers, e.g. poly(N-isopropylacrylamide) (PNIPAM) [69], and liquid-crystal elastomers (LCEs) [68,70], which are discussed in the following paragraphs.

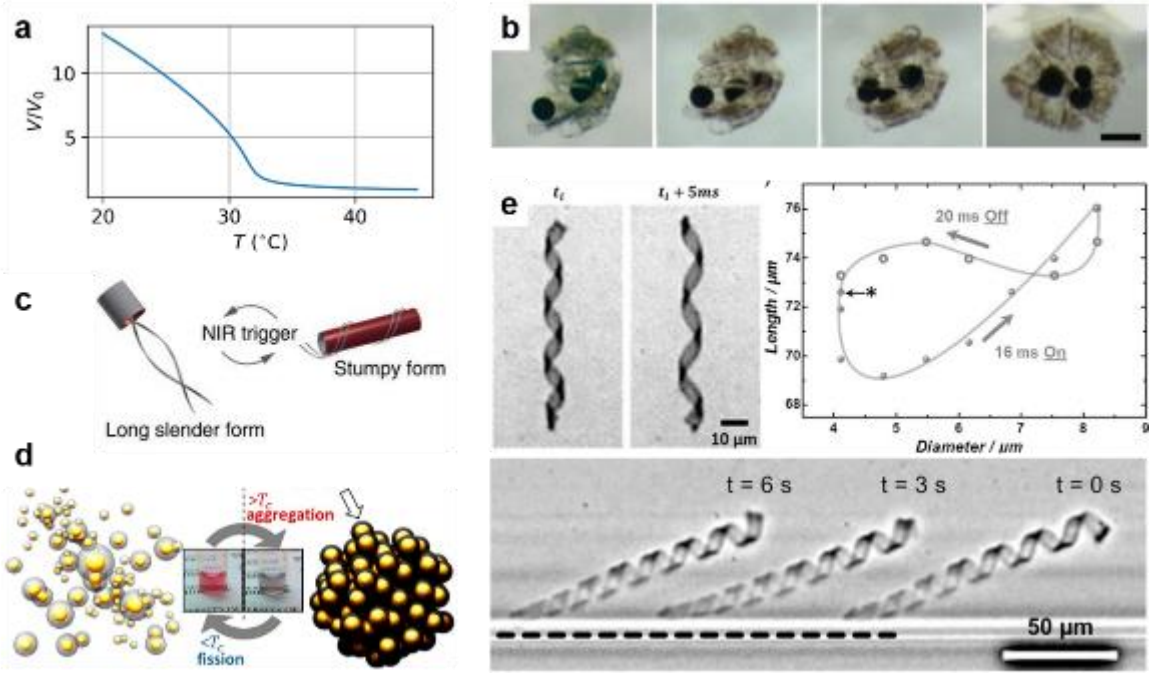

Figure 6. PNIPAM-based microrobots. (a) Temperature-dependent volume change of a PNIPAM hydrogel simulated according to equation (4) for $\phi_0 = 0.7$, $A = -7$, $\Theta = 33.5°C$, $N_x = 300$, and $\chi_1 = 0.5$. (b) PNIPAM hydrogel based microrobot closing up and grabbing alginate magnetic beads by cooling (scale bar: 200 µm). The subsequent release of the beads is powered by light (Reproduced with permission.[69] Copyright 2013, WILEY-VCH Verlag GmbH & Co. KGaA, Weinheim). (c) Reconfigurable microrobot: the microrobot moves by magnetic fields and its PNIPAM-powered shape reconfiguration is triggered by NIR light (Adapted under the terms of the CC BY license.[64] Copyright 2016, The Author(s)). (d) Nano-actuators consisting of PNIPAM-coated gold nanoparticles. The actuation and particle aggregation can be triggered by light via plasmonic heating (Reproduced with permission.[71]). (e) Helical microrobots based on PNIPAM hydrogel doped with gold nanorods and actuated via plasmonic heating. The out-of-equilibrium fast actuation leads to non-reciprocal deformation and thus locomotion of the microrobots in a fluid (Adapted with permission under the terms of the CC BY-NC-ND license.[67] Copyright 2016, The Authors. Published by WILEY-VCH Verlag GmbH & Co. KGaA, Weinheim).

3.1.1. PNIPAM-based microrobots

Polymers with a lower critical solution temperature (LCST) exhibit a phase transition that causes a sudden change in the solvation state. They become insoluble or less soluble upon heating. In water-based systems, the change in the hydration state of LCST polymer molecules is caused by the intra- and intermolecular hydrogen bonding taking precedence over the solubilization by water [72]. PNIPAM is a LCST polymer that has a transition temperature of about 32 °C in water and, consequently, a volume phase transition from a hydrated to a dehydrated phase upon heating. PNIPAM-based hydrogels heated above the LCST thus exhibit a macroscopic and reversible volume change (shrinkage) (Fig. 6(a)). Indeed, a hydrogel

consists of a polymeric mesh swollen by water due to osmotic pressure, and the swelling equilibrium is altered by the temperature change.

In the case of PNIPAM, the osmotic pressure Π consists of two components, one due to the mixing free energy (Π_m) and one due to the elastic free energy (Π_{el}) [73,74], which can be expressed as:

$$\Pi_m = -\frac{k_B T}{a^3}\,[\phi + \log(1-\phi) + \chi\phi^2], \tag{1}$$

$$\Pi_{el} = \frac{k_B T}{a^3}\frac{\phi_0}{N_x}\left[\frac{1}{2}\frac{\phi}{\phi_0} + \left(\frac{\phi}{\phi_0}\right)^{\frac{1}{3}}\right], \tag{2}$$

where k_B is the Boltzmann constant, T is the absolute temperature, a^3 is the volume for which the free energy contribution is defined, N_x is the degree of polymerization of the sub-chain between crosslinking points, and χ is the Flory interaction parameter, which can be approximated by:

$$\chi = \chi_0 + \chi_1\,\phi = \frac{1}{2} - A\left(1 - \frac{\Theta}{T}\right) + \chi_1\,\phi, \tag{3}$$

where χ_0 and χ_1 are the zeroth- and first-order terms of the parameter, $A = \frac{2\Delta S + k_B}{2k_B}$, and $\Theta = \frac{2\Delta H}{2\Delta S + k_B}$ is the Θ-temperature ($\Theta \gtrsim$ LCST; ΔS and ΔH the changes in entropy and enthalpy, respectively) [73].

The swelling state of the polymer is described by ϕ and ϕ_0, which are the volume fractions of the polymer in the hydrogel in the current and the initial unswollen state, respectively. The equilibrium volume fraction ϕ at a given temperature T can be obtained by setting $\Pi = \Pi_m + \Pi_{el} = 0$. The temperature-driven volume fraction change is then related to the volume change by the following simple equation:

$$V(T) = V_0\,\frac{\phi_0}{\phi(T)}\,. \tag{4}$$

Figure 6(a) shows the volume change calculated assuming that $\phi_0 = 0.7$, $A = -7$, $\Theta = 33.5$°C, $N_x = 300$, and $\chi_1 = 0.5$.

One of the first uses of PNIPAM in microrobotics was for magnetic microrobots with controlled drug-release functionality [66]. The microrobots consisted of beads of thermo-sensitive PNIPAM hydrogels containing magnetic nanoparticles (iron cobalt). The hydrogel beads were fabricated with alginate gel beads as a template. The NIPAM monomer, the cross-linker, the accelerator and the magnetic nanoparticles were mixed into an alginate solution. The mixture was added to a hardening solution containing a buffer, the NIPAM polymerization initiator, and $CaCl_2$. The Ca^{2+} ions in the solution caused the alginate molecules to form hydrogel beads instantly, in which the polymerization and gelation of the NIPAM then occurred. Finally, the hydrogel beads were kept in a phosphate buffer solution to chelate the Ca^{2+} ions and extract the alginate molecules from the beads, leaving the desired PNIPAM hydrogel beads. Increasing the temperature from 30°C to 36°C, the authors observed a volume reduction of 34%. The transition temperature could also be adjusted by adding a small percentage of hydrophilic acrylic acid monomers, such as to achieve an LCST higher than the body temperature. The embedded magnetic nanoparticles allowed for both magnetic pulling of the microrobots by quasi-static magnetic fields, and the microrobots' deswelling (intended for controlled drug release purposes) by inductive heating via an AC field. Inside a 4 kA/m, 160 kHz AC magnetic field, the microrobots achieved a temperature change of 2°C, corresponding to a 25% volume change, in 900 s (that is, 15 minutes) [66].

Light allows for a much faster triggering of the thermomechanical response of PNIPAM gels with respect to magnetic fields, provided that the gels are loaded with light-absorbing molecules or nanoparticles. Photo-responsive PNIPAM-based microrobots were realized that release microbeads upon the exposure to near infrared (NIR) light [69]. The microrobots were formed by a bilayer hydrogel, consisting of a passive 10-μm poly(ethylenglycol) diacrylate (PEGDA)

layer and a light-responsive 30-μm layer of PNIPAM-graphene oxide composite hydrogel. The bilayer was used to wrap iron oxide-loaded microbeads, as it closed upon them by swelling the PNIPAM layer at room temperature (Fig. 6(b)). Upon irradiation by a 785-nm laser, the bilayer opened up by differential deswelling of the two layers and released its load. The authors reported full deswelling in a matter of seconds with a graphene oxide content of 3 wt% and a NIR laser power of 1.5 W, as well as in a few minutes at a laser power of 0.7 W. The NIPAM was copolymerized with a small amount of the hydrophilic monomer acrylamide (AAm), such as to achieve a transition temperature of about 38°C. A similar (PEGDA-PNIPAM) bilayer structure was adopted to develop magnetic microrobots whose morphology was reconfigured by a NIR light trigger [64] (Fig. 6(c)). In this case, light absorption was performed by the embedded magnetic nanoparticles, rather than by graphene oxide. The systems reported above rely on magnetic field for locomotion, whereas the slow PNIPAM response is used for additional functionalities.

Very fast and strong PNIPAM-based actuation was instead achieved by plasmonic absorption of an incident laser by nanoparticles. For instance, nanoactuators that respond within a microsecond and generate forces of several nN were developed based on PNIPAM-coated gold nanoparticles [71]. The particles were formed by functionalizing citrate-stabilized gold nanoparticles (60 nm in diameter) with PNIPAM via ligand exchange above the LCST. At room temperature, the nanoparticles spontaneously formed aggregates when heated above the LCST. When cooled down to room temperature, the particles repelled each other and spontaneously dispersed again in the solution (Fig. 6(d)). Nano-actuators were built by particle clusters encapsulated in a 70-nm-thick agarose film, and the authors report switching in less than 2 μs and the generation of forces of about 100 nN on cooling and expansion.

Similarly, fast-actuation PNIPAM-based microrobots were obtained by exploiting plasmonic heating via embedding engineered gold nanorods in the hydrogels, enabling light-induced

locomotion. Helical microrobots were obtained from thin (about 1 μm) PNIPAM hydrogels loaded with gold nanorods having a longitudinal plasmon absorption peak at 791 nm at a concentration of 9 nanorods per cubic micrometer [67]. The gel-based microrobots were fabricated by carrying out the gelation reaction of a dimethyl sulfoxide (DMSO) solution of NIPAM monomers, crosslinker, photoinitiator, and gold nanorods (grafted with poly(ethylene glycol) – PEG) in micromolds. To obtain microrobots with a helical shape, gel stripes (as prepared in the molds) were coated with a gold layer of a few nanometers (which only slightly enhanced the heating effect, as the plasmon resonance of the gold skin was shifted to lower wavelengths). The DMSO-based gels were then placed in cold water and swelled by about 60% in the lateral dimension and, in the case of gold-coated ones, they spontaneously bent into a helical shape (with a 5-fold volume expansion and the gold layer facing the inner side of the helix). The helical microrobots were actuated by periodically turning on and off a 808-nm laser with a power density of 1.7 W/mm^2, achieving reversible actuation with an on-time $t_{on} = 16$ ms and an off-time $t_{off} = 20$ ms. In each cycle the microrobots underwent contraction (volume change) and bending, resulting in both a diameter and length change of the helices (Fig. 6(e)). In spite of the small size of the microgels, the authors demonstrated out-of-equilibrium heating driven by the highly efficient plasmon resonance absorption. This resulted in non-reciprocal deformation of the microrobots, that is, the expansion and shrinkage between the swollen and unswollen states took two different paths (Fig. (e)). Non-reciprocal motion is needed for swimming at low Reynolds numbers, i.e. at the microscale in water [75]. The authors demonstrated translational motion along a wall of a helical microrobot undergoing non-reciprocal deformations driven by out-of-equilibrium plasmonic heating (Fig. 6(e)). Light-driven microrobotic locomotion has also been achieved in microrobots consisting of photoresponsive LCEs, as reported in the following sections.

3.1.2. LCEs-based microrobots

Liquid-crystal elastomers are rubber-like materials consisting of polymeric networks of liquid-crystal monomers (or mesogens). As for PNIPAM hydrogels, LCEs also undergo a temperature-dependent phase transition, which can also be triggered by light when the elastomers are loaded with a photoresponsive chromophore. Contrary to the hydrogels, however, the LCEs' phase transition results in an isovolumetric change in shape, rather than in a volume change.

At room temperature, the liquid-crystal molecules within an LCE polymeric network are in an ordered phase, for instance they possess orientational order (nematic phase). In nematic LCEs the liquid-crystal rod-like molecules are aligned along a common orientation, known as the nematic director $\hat{n}$. The degree of orientational order of the liquid-crystal molecules can be described by the nematic order parameter Q. Assuming that each molecule is oriented with an angle θ with respect to the nematic director $\hat{n}$, the nematic order parameter Q is defined via the average of the second Legendre polynomial [76], that is

$$Q = \langle P_2(\cos\theta) \rangle = \left\langle \frac{3}{2}\cos^2\theta - \frac{1}{2} \right\rangle, \tag{5}$$

where the angle brackets $\langle ... \rangle$ indicate the average over the liquid-crystal molecule direction θ. According to this definition, $Q = 1$ corresponds to a perfectly ordered state, where all molecules are exactly aligned along $\hat{n}$ ($\theta = 0$ or π), whereas $Q = 0$ denotes a completely disordered state, with all molecules aligned randomly (isotropic phase). Nematic LCEs undergo a temperature-dependent transition from a nematic phase, with $Q = Q_N \leq 1$, to an isotropic phase, with $Q \approx 0$. The dependence of Q on the temperature T can be described by an empirical sigmoidal function of the kind:

$$Q(T) = Q_N \left(1 + e^{\frac{T - T_{NI}}{\gamma}}\right)^{-1}, \tag{6}$$

where Q_N is the order parameter in the reference nematic phase, T_{NI} is the nematic-to-isotropic transition temperature and γ is a constant related to the sharpness of the transition. Figure 7(a)

shows an example of the temperature-dependent trend of the order parameter Q for $Q_N = 0.4$, $T_{NI} = 80$°C, and $\gamma = 4$°C.

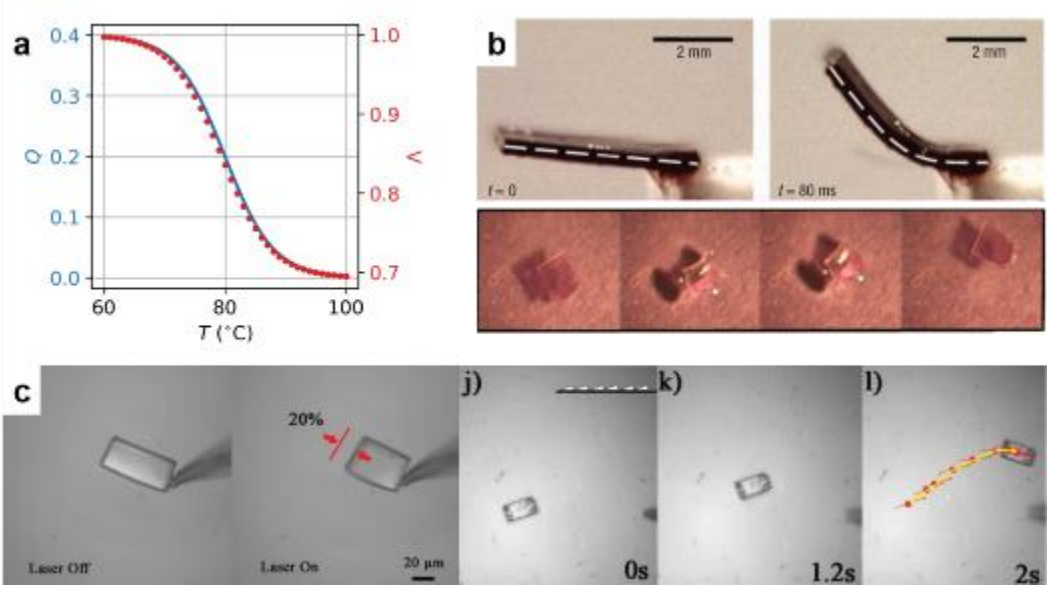

Figure 7. LCE-based microrobots. (a) Temperature-dependent change in order parameter Q and corresponding longitudinal stretch Λ of an LCE simulated according to equations (6) and (7) for $Q_N = 0.4$, $T_{NI} = 80$°C, and $\gamma = 4$°C. (b) Dye-doped LCEs that can be triggered by light. Top: photoresponsive LCE that bends under asymmetric illumination (light from the top). Bottom: photoresponsive LCE suspended on a fluid that deforms and moves away from the light spot (Adapted with permission.[77] Copyright 2004, Nature Publishing Group). (c) Azo-dye-containing microfabricated LCE. The azo-dye absorbs green light and the LCE undergoes reversible photothermal shape change (up to 1.8 kHz). A micro-walker consisting of an LCE with microfabricated rigid legs shows light-fueled directional motion commanded by a surface grating (Adapted with permission under the terms of the CC BY-NC license.[68] Copyright 2015, The Authors. Published by WILEY-VCH Verlag GmbH & Co. KGaA, Weinheim).

The temperature-dependent change in the order parameter drives a constant-volume shape change of the elastomer consisting of a longitudinal contraction along $\hat{n}$ accompanied by an expansion in the plane perpendicular to $\hat{n}$. The length (along $\hat{n}$) of an LCE sample can be expressed as $L(T) = L_N\,\Lambda(T)$, where L_N is the LCE length in the nematic phase and $\Lambda(T)$ is the temperature-dependent stretch of the material, defined as [76]

$$\Lambda(T) = \frac{L(T)}{L_N} = \left(\frac{1+2Q(T)}{1-Q(T)}\right)^{\frac{1}{3}} \left(\frac{1+2Q_N}{1-Q_N}\right)^{-\frac{1}{3}}. \qquad (7)$$

An example of temperature-driven LCE contraction calculated based on the parameters Q_N, T_{NI}, and γ with the values given above is shown in Fig. 7(a).

To trigger the LCE phase transition by light, the elastomers can be loaded with photoabsorbing chromophores or particles [78]. One popular class of molecules used to this purpose are azo-benzene dyes, which can be covalently linked to the elastomer's polymeric network. These azo-benzene mesogenes normally have a rod-like shape (*trans* isomer) and bend on absorbing a photon (*cis* isomer). The *trans*-*cis* photoisomerization reduces the molecular order within the liquid crystalline material (by a build-up of the bent *cis*-isomer population) and can thus trigger the nematic-to-isotropic phase transition at low temperature (lower than in the absence of the light stimulus). In other words, an azo-dye-functionalized LCE under illumination has an effective temperature (by which we can predict the change in order parameter and the associated contraction from equations (6) and (7), respectively) that is higher than the actual temperature [76]. In a purely opto-mechanical material system, the nematic-to-isotropic transition is obtained upon illumination with almost no increase in the actual temperature. Common azo-dye mesogens show an absorbance peak for the *trans* isomer in the UV region; the *cis* isomer is instead metastable and typically switches back spontaneously by a temperature increase, or by illumination by a different light source (typically in the yellow region). Whereas the time required for an opto-mechanical LCE to reach the nematic-to-isotropic transition depends on the intensity of the UV light source, the spontaneous back-transition is typically slow (in the range of hours), or it requires an additional light source, making these materials not ideal for reversible actuators in microrobotics.

Fast periodic responses were observed for LCEs doped (rather than functionalized) with azo-dyes with a *trans* absorption peak in the visible region of the spectrum [77] (Fig. 7(b)). The LCE samples (320 μm-thick), powered by a 514 nm, 600 mW laser showed a characteristic rise time of 20 ms and a characteristic relaxation time of 75 ms. The authors attributed the LCE response to either laser heating or photoisomerization-induced reduction of orientational order, and probably both phenomena play a role. They also demonstrated 5-mm-diameter LCE disks

floating on the surface of water that, under illumination with peak intensity of 1.1 W/cm^2, spontaneously moved away from the light source (see Fig. 7(b)).

Zeng *et al.* 3D-printed microscale LCE structures by 2-photon lithography that contained a modified azo-benzene mesogen with a peak absorption in the green region of the spectrum, (thus decoupling the dye absorption and the photo-initiator absorption) [79]. The azo-dye also have the advantage that its *cis*-isomer is very unstable and thus the relaxation time of the LCE is very fast. Indeed, they demonstrated a remarkable actuation frequency of 1.8 kHz (for samples with size of 60×30×10 μm^3 in air) [68] (Fig. 7(c)). It is reasonable to assume that in such a system the main mechanism at play is the photothermal response (heating by laser absorption), and that the azo-dye mainly acts as the light-absorber. The authors developed an LCE-based microscopic walker fueled by light. The walking microrobot consisted of a microfabricated LCE body (with a size of 60×30×10 μm^3) with four conical legs made of commercial photoresist. The microrobot showed directional locomotion on a surface with a grating groove pattern, with the walking direction determined by the pattern (Fig. 7(c)). A slightly larger microrobot (100×50×10 μm^3) with different legs was able to perform jumps up to ~1 cm on a Teflon surface. The jumps were achieved by storing of the light energy in the elastic deformation until the adhesion with the surface was overcome and the elastic energy was suddenly released.

The photothermal response of a microscale LCE sample (or of an LCE-based microrobot) immersed in a fluid can be estimated with the help of the following expression:

$$\frac{\partial}{\partial t}[\rho\, c\, V\, (T - T_0)] = \eta I\, A_{proj} - h\, A_{sur}\left(T - T_f\right), \tag{8}$$

where for simplicity it is assumed that the microrobot's height is small compared to the penetration depth of the light in the LCE, i.e. that the laser heating is homogeneous along the height of the microrobot. Indeed, I is the incident light intensity (W/m^2) and η represents an overall light absorption efficiency (ranging from 0 to 1). A_{proj} and A_{sur} are the area of the

microrobot's projection on the workspace plane (i.e. the plane perpendicular to the incoming laser beam) and the surface area, respectively (in m^2). ρ, c, and V are the mass density (kg/m^3), specific heat capacity (J/kg/K) and volume (m^3) of the LCE microrobot, respectively, whereas T and T_0 are its current and initial temperature (K), and T_f is the bulk temperature of the fluid (K). Finally, h is the heat transfer coefficient of the microrobot in the fluid ($W/m^2/K$). Therefore, the left term in equation (8) represents the rate of change of the heat stored in the microrobot, whereas the first term on the right side represents the input power due to laser heating and the second term is the heat transfer towards the fluid (cooling).

The modeling of heat transfer by means of the lumped heat transfer coefficient h is based on the assumption that a thin thermal boundary layer δ_T forms around the object (where only heat conduction occurs, and where the average temperature is $T_{\delta_T} = \frac{T+T_f}{2}$) and that $\delta_T \ll l$, where l is a characteristic size of the object. In our microscale system, however, the thermal boundary layer is comparable to or larger than the size of the object, that is, $\delta_T \gtrsim l$. For this reason, a more accurate model of the photothermal response of an LCE-based microrobot also takes into account the thermal inertia of the boundary layer, such as:

$$\frac{\partial}{\partial t}\left[\rho c V (T - T_0) + \rho_f c_f V_{\delta_T} (T_{\delta_T} - T_f)\right] = \eta I \, A_{proj} - h \, A_{sur} \left(T - T_f\right), \qquad (9)$$

where ρ_f and c_f are the mass density and specific heat capacity of the fluid, respectively, and V_{δ_T} is the volume of the boundary layer around the object. The boundary layer can be estimated as $\delta_T = l/Nu_l$ (where Nu_l is the average Nusselt number of the microrobot in the fluid). Therefore, the actuation of a photothermal LCE-based microrobot shows a complex dependence on its geometry and, especially, on its environmental condition.

3.2. Soft microrobots controlled by structured light

In this section we summarize results on the development of soft microrobots based on photothermal LCEs and controlled by structured light. The fast and reversible actuation of

photothermal LCEs make them ideal for realizing light-controlled microrobots, as they can achieve large deformations at relatively high frequencies with only one light source as a control means. In Ref. [70] we found that they can also be powered in a selective manner (that is, it is possible to selectively photoactuate parts of the microrobot) by spatially modulating the control light field. This allowed us to achieve complex movements and sophisticated self-propulsion in microrobots with an extremely simple design and geometry. The main advantage of this approach consists in that a simple microrobot (made just of a homogeneous piece of LCE material) can be controlled to perform many different movements and gaits, as if it consisted of many independent microactuators, and can thus adapt to execute different tasks and to move in different environments.

3.2.1. Structured light

Modulating the light field intensity in both time and space is essential to achieve controlled complex body-shape deformations in a monolithic photothermal LCE. To do so, we used a digital micromirror device (DMD) [70] (Fig. 8(a)). The DMD consists of an array of about 800,000 micromirrors, each controlling the reflection of a portion of the incoming laser beam (532 nm, up to 10 W) and each representing a pixel in the projected light field. The micromirrors can be switched dynamically (up to kHz) and the projected light field can be controlled via software by uploading sequences of binary and grayscale images onto the DMD module. One advantage of the generation of light fields by a DMD compared to systems like scanning beams controlled by moving mirrors (e.g. see Ref. [33]) is that all light pixels are projected in parallel. One problem with DMD-based systems is, however, that, when illuminated with a coherent laser light beam, diffraction losses occur (as the DMD behaves as a regular grating) and the resulting efficiency is lower compared to illumination with a non-coherent light source like an LED. The apparatus we developed has an overall optical efficiency η_{opt} (defined as the ratio between the projected optical power P_{proj} and the nominal laser

source output power P_{laser}) of about 30%. In the ideal case of homogenous illumination of the workspace (with area A_{ws}), which we ensure by shaping the beam upstream of the DMD, the light intensity (W/m^2) is constant and given by $I_0 = \eta_{opt} P_{laser}/A_{ws}$. By modulating the laser beam by the DMD, the projected light field intensity can be expressed as $I(x, y, t) = I_0\, p(x, y, t)$, where $p(x, y, t)$ is the modulation function with values ranging from 0 to 1.

The light fields we used to control the actuation and locomotion of soft LCE-based microrobots are examples of structured light, that is, they consist of regular (and usually binary) light patterns. In particular, they can be defined as two-dimensional rectangular traveling waves:

$$p(x, y, t) = \frac{1}{2}\{1 + \mathrm{sgn}[\cos(k\, x \cos\varphi + k\, y \sin\varphi - \omega t) - \cos(\pi\, \delta)]\}, \qquad (10)$$

where $\mathrm{sgn}(\dots)$ is the sign function, $k = 2\pi/\lambda$ is the wave number (λ is the wavelength of the rectangular traveling wave – not the laser source wavelength), $\omega = 2\pi f$ is the radial frequency of the traveling wave, φ is its traveling direction in the two-dimensional workspace, and δ is its duty cycle (that is, the fraction of the period in which the light is actually on). Examples of structured light fields defined by equation (10) are shown in Fig. 8(b). The control parameters for the light field generation are the wavelength λ, the frequency f, the direction φ, and the duty cycle δ. The adoption of structured light thus greatly simplifies the microrobots' control problem, as it reduces the number of control parameters from about $8{\cdot}10^5$ (the number of individually controllable micromirrors) to only 4 parameters describing the rectangular traveling wave pattern.

3.2.2. Selective continuum actuation

In Ref. [70] we demonstrated that structured light can be used to selectively power the actuation of continuum soft microrobots consisting of monolithic photothermal LCEs. The microrobots' actuation can thus be controlled by the aforementioned structured light field parameters (λ, f, δ, φ). In particular, we have shown that the LCE's active deformation is localized to the regions

that are directly hit by light, and that the deformation dynamically follows the structured light field as this moves.

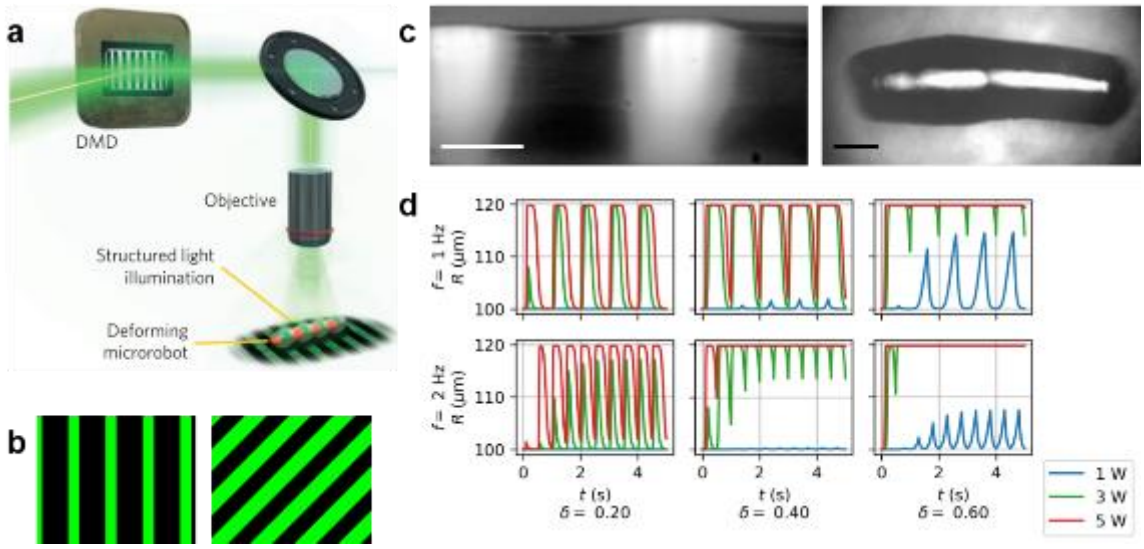

Figure 8. Soft microrobots actuation controlled by structured light. (a) Schematics of the microrobotics control by structured light fields generated by a DMD. Reproduced from [70]. (b) Examples of structured light fields (frames size: 1280×1024 px). Left: frame from a periodic structured light with $\varphi = 0$, $\lambda = 300$ px, and $\delta = 0.3$. Right: frame from a periodic structured light with $\varphi = \pi/4$, $\lambda = 250$ px, and $\delta = 0.5$. (c) Frames from periodic deformation of photothermal LCE-based microrobots controlled by structured light [70]. Left: top view (scale bar: 200 μm). Right: side view (scale bar: 100 μm). (d) Simulated response of a section of a cylindrical LCE microrobot (immersed in silicone oil) to a periodic light field, according to equation (14). The effect of frequency f, duty cycle δ, and laser power P_{laser} are investigated, and cases of under- and over-actuation are shown.

Figure 8(c) shows the side view of a cylindrical microrobot of radius $R \approx 100$ μm powered by a structured light field with wavelength $\lambda \approx 260$ μm, frequency $f = 1$ Hz, and duty cycle $\delta = 1/3$. The top view of the actuation of another microrobot ($R \approx 170$ μm) is also shown in Fig. 8(c) (structured light parameters: $\lambda \approx 950$ μm, $f = 1$ Hz, $\delta = 1/3$). In both cases, the microrobot consisted of a cylindrical photoresponsive LCE with the nematic director $\hat{n}$ parallel to the longitudinal axis of the cylinder, resulting in longitudinal contraction accompanied by radial expansion upon illumination by green light [70].

The LCE microrobots were fabricated from a mixture containing 85 mol% of a side-on acrylate mesogen, 13 mol% of crosslinker (1,6-Hexanediol diacrylate), 1 mol% of UV photoinitiator, and 1 mol% of the green-absorbing azo-benzene dye developed in Ref. [79]. A piece of the solidified, uncured mixture was placed on a glass slide and heated above the nematic-to-

isotropic transition temperature ($T > 80$°C, thus melting it). The mixture droplet was then cooled down until it became viscous enough to pull a continuous fiber by a tip. While pulling, the fiber was cured with an ultraviolet lamp. The pulling stress during fabrication was responsible of aligning the mesogens along the fibers' longitudinal axis. To obtain microrobots, the fibers were cut with a scalpel into cylinders of about 1 mm. The nematic order of the cylindrical LCEs was characterized by Small-Angle X-ray Scattering (SAXS) [70]. By fitting equation (6) to the experimental data we estimated $Q_N = 0.396$, $T_{NI} = 83.2$°C, and $\gamma = 4.3$°C. To better understand how the light control parameters influence the LCE microrobots' actuation we can use the photothermal response reported in equation (9) in the case of a structured light intensity field described by equation (10). In the case of cylindrical microrobots of radius R and length L placed horizontally in the workspace, and assuming $L \gg R$ and $T_0 = T_f$, we can rewrite equation (9) as:

$$\begin{aligned} &\frac{\partial}{\partial t}\left[\rho c V\left(T - T_f\right) + \rho_f c_f V_{\delta_T}\left(T_{\delta_T} - T_f\right)\right] = \\ &= \frac{\partial}{\partial t}\left[\left(\rho c + 2\rho_f c_f\left(\frac{1}{Nu_D} + \frac{1}{Nu_D^2}\right)\right)\pi R^2 L\left(T - T_f\right)\right] \\ &= \frac{\partial}{\partial t}\left[(\rho c)^*\,\pi R^2 L\left(T - T_f\right)\right] = 2RL\left[\eta\, I(x,y,t) - \pi h\left(T - T_f\right)\right], \end{aligned} \tag{11}$$

where Nu_D is the microrobot's average Nusselt number in the fluid (with $D = 2R$), and $(\rho c)^*$ represent the volumetric heat capacity of the system including both the microrobot and the boundary layer. Considering that the volume $V = \pi R^2 L$ of the LCE microrobot is constant (isovolumetric deformation), we can further simplify the above expression, to obtain:

$$\frac{\partial}{\partial t}\left[(\rho c)^*\left(T - T_f\right)\right] = \frac{2}{\pi R}\left[\eta\, I(x,y,t) - \pi h\left(T - T_f\right)\right]. \tag{12}$$

It is worth noticing that the length of the microrobot cancels and that the radius actually depends on the local temperature, namely:

$$R = R(T) = R_N\,\Lambda(T)^{-\frac{1}{2}}, \tag{13}$$

where R_N is the radius of the microrobot in the nematic phase (at room temperature) and $\Lambda(T)$ is the stretch function defined in equation (7).

Equation (12) thus approximates the temperature dynamics of each section of the microrobot (heat transfer within the microrobot is neglected), and it can be further simplified by assuming that, in a first approximation, the term $(\rho c)^*$ does not change, leading to:

$$\frac{\partial T}{\partial t} = \frac{2}{\pi(\rho c)^* R(T)}\left[\eta\, I(x,y,t) - \pi h \left(T - T_f\right)\right]. \tag{14}$$

From this equation we can estimate the minimum intensity $I_{0,min}$ required to heat the microrobot to the transition temperature T_{NI}, and the maximum actuation frequency f_{max} considering the characteristic cooling time τ_c:

$$I_{0,min} = \frac{\pi h \left(T_{NI} - T_f\right)}{\eta}, \qquad f_{max} \sim \tau_c^{-1} = \frac{h}{(\rho c)^* R}. \tag{15}$$

The results shown in Fig. 8(c) were obtained with the structured light rectangular wave traveling parallel to the longitudinal axis of the cylindrical LCE microrobots. It follows that each thin slice of the cylindrical microrobot is excited by an intermittent light stimulus of intensity I_0, frequency f, and on-time $t_{on} = \delta/f$. Therefore, whereas the peak power absorbed by the LCE only depends on the light intensity and thus on the laser power, namely $P_{peak} \propto P_{laser}$, the average absorbed power (over one period of actuation) also depends on the duty cycle δ, that is, $P_{avg} \propto \delta\, P_{laser}$. Examples (obtained from the numerical solution of equation (14)) of the complex dependence of the photothermal actuation of a slice of a cylindrical LCE microrobot on the laser power P_{laser}, the frequency f, and the duty cycle δ are shown in Fig. 8(d). It can be seen that an optimal combination of the parameters exists that allows a maximum reversible actuation of the LCE-based microrobots, whereas non-optimal combinations can lead to either *under-actuation* (the maximum deformation is not achieved) or *over-actuation* (the maximum deformation is achieved but the initial shape is not recovered within the actuation period, resulting in sub-optimal actuation amplitude).

Experiments and numerical simulations have elucidated the role of another control parameter, that is, the wavelength of the light structures λ [70,80]. Obviously, λ controls the spatial periodicity of the microrobot deformation. However, we have shown that exciting cylindrical LCE microrobots with structured light patterns with $\lambda \lesssim R$ results in sub-optimal actuation, and that this is mainly due to the continuity and mechanical properties of the microrobots' body. This behaves as a low-pass filter in the spatial frequency domain, with the spatial frequency defined as $\nu = \lambda^{-1}$ [80]. That is, structured light fields with high spatial frequencies (i.e. short wavelength/narrow features) do not induce correspondingly high spatial frequency actuation, but instead result in smoothed, low-amplitude deformations. Moreover, sharp transitions in the light field (which is defined as a binary field, according to equation (10)), that are associated with high spatial frequencies, are also smoothed out, resulting in continuous deformation profiles. In Ref. [80] we evaluated a 'spatial frequency response', SFR, of the LCE microrobots' body from mechanical numerical simulation, by which it is possible to accurately predict the deformation profile of the microrobot from the spatial frequency content of the input structured light field. Importantly, as a consequence of the filtering or smoothening behavior of the microrobots' body, the microrobots cannot achieve arbitrarily fine deformation patterns in spite of the very high spatial resolution of the light field. This has an effect on the microrobots' locomotion, as explained in the following section.

3.2.3. Biomimetic swimming

We have seen in the previous sections that micromotors are characterized by the fact that they can transduce some input energy (usually chemical) into mechanical energy (i.e. motion) by phenomena such as self-diffusiophoresis, whereas microrobots are usually driven by external fields (e.g. magnetic fields) that directly exert forces and or torques on their body. Microorganisms instead move in liquids by *swimming*, that is, they self-propel by internally-generated periodic body-shape changes [81]. The soft microrobots consisting of photothermal

LCEs and controlled by structured light were the first *swimming* microrobots [70] that self-propelled in liquids (with no external propulsive forces or torques) by periodic body-shape changes alone – and thus swim like biological microorganisms.

As discussed in the previous section, structured light can be used to induce traveling wave deformations in continuous soft microrobots consisting of monolithic photothermal LCEs. Such motion patterns actually mimic the behavior of ciliates, a group of microorganisms that possess thousands of thin hairs, or cilia. The asynchronous coordinated beating of the cilia results in surface waves that travel along the microorganism's body, also known as metachronal waves. In the case of the LCE-based soft microrobots, the surface waves are obtained by the light-controlled actuation of the LCE body, which dramatically simplifies the microrobots' design, fabrication, and control compared to trying to realize thousands of tiny appendages beating in a controlled, coordinated fashion. Indeed, we demonstrated that, in spite of their highly simplified bioinspired design, LCE cylinders powered and controlled by structured light can *swim* in a liquid [70]. In particular, an LCE cylinder ($R_N = 120$ μm and $L_N = 1.23$ mm) was suspended in the bulk of a liquid by creating a mass density gradient in the fluid, composed of two miscible liquids (glycerol and water). By projecting structured light fields having $\lambda = 390$ μm, $f = 2$ Hz and $\delta = 1/3$, the LCE-based microrobot generated sustained peristaltic deformations and thus moved opposite to the traveling wave direction at a speed of about 2.5 μm/s (see Fig. 9(a)).

Compared to ciliates, which are about 200 μm in length yet can swim at more than 1 mm/s (in the case of *Paramecium*), the artificial microrobots were much slower. This stark difference is mainly due to the limitations of the LCEs' photothermal response. In particular, the swimming speed of both ciliates and artificial microrobots propelled by peristaltic motions in first approximation depends on the wave amplitude squared, on the frequency (linearly), and on the reciprocal of the wavelength. Whereas in the case of long wavelengths the wave amplitude of

the artificial microrobots is comparable to that of cilia-powered microorganisms, the maximum actuation frequency of the photothermal LCE in the liquid is limited to a few Hz (see Fig. 8(d)), whereas cilia beat at several tens of Hz (and up to one hundred). In addition, given the reciprocal dependence of the swimming speed on the wavelength, short wavelengths ideally result in faster locomotion – indeed, typical wavelengths in ciliates' metachronal waves are on the order of tens of microns. In the LCEs, instead, because of the smoothening of the deformation occurring at short wavelengths, these are associated with small wave amplitude, which leads to low swimming speeds. Nonetheless, the locomotion of the structured light-controlled LCE microrobots qualitatively mimics that of ciliates.

The cilia in ciliated microorganisms perform an asymmetric, non-reciprocal motion, and their tips follow a roughly ellipsoidal path. Each point on the surface of a structured light-controlled microrobot also perform a similar non-reciprocal ellipsoidal motion, which can be decomposed in a longitudinal and a transversal oscillation. The surface motion can thus be described by the surface coordinated r_s and z_s approximately given by

$$r_s = r_0 + a\sin(kz - \omega t) \tag{16}$$

$$z_s = z + b\cos(kz - \omega t) \tag{17}$$

where the medium radius $r_0 = R_N\left(1 + \Lambda_{NI}^{-\frac{1}{2}}\right)/2$, with Λ_{NI} being the maximum, nematic-to-isotropic stretch of the LCE, and, because the LCE deformation occurs at constant volume [70], $b = \frac{2a}{kr_0}$. In the case of full actuation amplitude (i.e. at wavelengths $\lambda > R_N$, see section 3.2.2), the transversal amplitude $a \equiv a_{max} = R_N\left(\Lambda_{NI}^{-\frac{1}{2}} - 1\right)/2$ and the longitudinal amplitude $b \equiv b_{max} = \frac{2\,a_{max}}{k\,r_0} = \frac{\lambda}{\pi}\left(\Lambda_{NI}^{-\frac{1}{2}} - 1\right)/\left(\Lambda_{NI}^{-\frac{1}{2}} + 1\right)$. For shorter wavelengths and sub-optimal

actuation, the transversal amplitude can be calculated as $a \approx a_{max}\left[1 - e^{-\left(\frac{\lambda}{\lambda_c}\right)^{\alpha}}\right]$, where λ_c is the critical wavelength for the smoothening effect and α is a fitting parameter.

Apart from the smoothing which occurs at short wavelengths, the transversal amplitude of deformation is constant, i.e. it only depends on the LCE size and its nematic-to-isotropic maximum stretch, whereas the longitudinal amplitude of deformation linearly depends on the wavelength. This means that, depending on the wavelength of the structured light pattern, the elliptical path followed by the points on the LCE surface changes its aspect ratio. This has a counterintuitive effect on the swimming speed. In particular, the transversal component of the peristaltic wave deformation is associated with a *positive* swimming velocity (i.e. antiparallel to the wave traveling direction), whereas the longitudinal component contributes to *negative* swimming velocities (parallel to the wave traveling direction). As the wavelength of the structured light pattern increases, the longitudinal component of the periodic deformation gains importance with respect to the transversal component, and the swimming velocity turns from positive to negative. That is, at short-medium wavelengths the microrobots swims in the opposite direction with respect to the traveling wave of deformation, whereas at long wavelengths it swims parallel to the traveling wave direction (Fig. 9(a)). This reversal in the swimming direction, given by the aspect ratio of the surface point non-reciprocal path, recalls the different kinds of metachrony exhibited by ciliated microorganisms (symplectic and antiplectic metachrony).

Soft microrobots consisting of simple monolithic LCEs can thus exhibit sophisticated biomimetic movements and achieve microorganisms-like swimming when powered and controlled by structured light. The main advantage of this approach is that the movements are not pre-programmed in the material, rather they can be tuned in a wide range by simply

changing the structured light field. This gives this kind of microrobots an unparalleled versatility, as discussed in the next section.

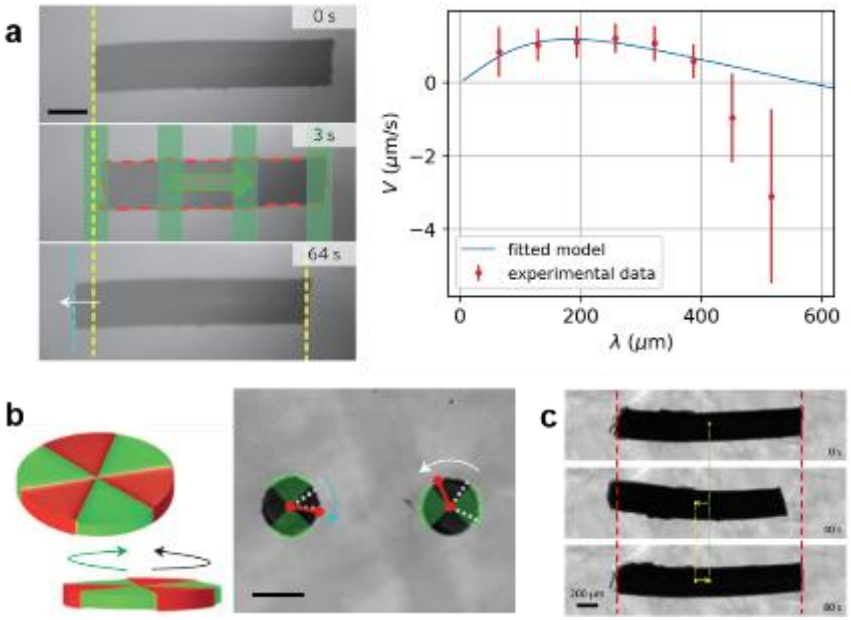

Figure 9. Locomotion of structured light-controlled soft microrobots consisting of photothermal LCEs. (a) Soft microrobot swimming in the bulk of a liquid by traveling-wave deformations. Left: frames from a swimming experiment with structured light overlay (scale bar: 200 μm). Right: summary of swimming experiments showing velocity reversal for long wavelengths. Adapted from [70]. (b) Rotating disk-shaped microrobots controlled by structured light consisting of azimuthal rectangular waves [70]. Left: simulated deformation of a microrobot. Right: two independently rotating microrobots (scale bar: 200 μm). Adapted from [70]. (c) Light-controlled LCE-based microrobot moving inside a gel. Reproduced with permission.[82] Copyright 2017, IEEE.

3.2.4. Versatile locomotion

The complex movements of the LCE-based soft microrobots are directly controlled by the structured light field. Tuning the parameters of the structured light rectangular wave not only allows us to ensure proper actuation performance, as discussed in section 3.2.2, but also to change the microrobots' gait, thus achieving different kinds of locomotion and making individual microrobots adapt to move in different environments.

Simple LCE disk-shaped microrobots (thickness: 50 μm, diameter: either 200 or 400 μm) with axial nematic director were controlled by linear rectangular-wave light patterns (as defined in equation (10)), resulting in translational movement in the two-dimensional workspace [70]. The disks changed their movement direction by changing their heading rather than by turning. This

was achieved by simply changing the wave traveling direction φ of the structured light field. In addition, rotating azimuthal (fan-shaped) light fields were projected centered on the disk microrobots. The obtained rotating deformations resulted in the controlled in-place rotation of the disks (see Fig. 9(b)). Different kinds of waves therefore lead to different movement capabilities.

Cylindrical LCE microrobots powered by linear rectangular-wave light fields vary their locomotion performance based on the wave parameters, as discussed for the influence of the wavelength λ in the case of swimming. It must be highlighted that both the actuation performance (as discussed in section 3.1.2) and the optimal gait for locomotion change based on the environment. For example, in Ref. [80] we showed that the dependence of the locomotion speed on the wavelength λ and duty cycle δ for moving on the bottom of a liquid-filled container is different than that for moving in the bulk of the fluid. Also, the deformation pattern of a cylindrical LCE microrobot was tuned to achieve displacements inside an agarose hydrogel [82] (see Fig. 9(c)). In Ref. [83] we used probabilistic machine learning to find the optimal gait for microrobots moving on the bottom (giving maximum locomotion speed) by automatically tuning the wavelength λ and duty cycle δ. This learning control approach more than doubled of the locomotion speed of the microrobot with respect to an informed initial guess within a predefined number (twenty) of automated experiments. This approach enables automatic optimization of the microrobots performance in unknown environments (without prior locomotion models) with a predefined experimental budget (the number of experiments that it is allowed to run) and being robust with respect to variability among microrobots.

In summary, combining soft photoresponsive materials with structured light control thus results in an unmatched level of movement versatility in microrobotics.

4. Conclusion

Light is currently one of the most versatile approaches to wirelessly power and control mobile microscale devices based on photocatalytic and photomechanical materials. The adoption of light enables an unprecedented control over the movement of such microdevices, and the discovery of new phenomena in active matter systems. Light is also used to realize microrobots that can mimic behaviors of biological microorganisms. Indeed, the ability to modulate light in both time and space, allows one to develop active matter and microrobotic systems that can locomote and interact and give rise to a rich phenomenology. The exploitation of high resolution, multi-wavelength light fields with complex modulation of intensity, phase, and polarization, will extend these capabilities and can for instance permit the selective addressing of individual micromotors in a crowded environment [32].

Light-based control of mobile microdevices also has some intrinsic limitations. For instance, whereas magnetic and acoustic fields can be used to control microobjects in three dimensions, light-based systems are mainly limited to two-dimensional control; nonetheless, we have shown that light can be used to induce out-of-plane motion in photocatalytic micromotors (see section 2.2). Moreover, light-based control requires that the workspace is optically accessible, that is, that the microdevices move in a clear transparent medium. This makes a number of applications, including medical applications in body tissues, extremely challenging. Innovative methods for light modulation and transmission in three-dimensional complex and scattering media are therefore highly sought.

Novel and improved materials are needed to enhance the functionality and widen the application spectrum of light-controlled micromotors and microrobots. Moreover, as the adoption of three-dimensional light fields and the optical power transmission through opaque media are likely to result in smaller light intensities available for actuation, the energy efficiency of microdevices will become a key issue. This mainly depends on the constituent

materials and on their coupling to the incoming photons. Materials that can efficiently respond to light with photo-triggered catalytic activity and mechanical deformation will therefore represent the key enabling technology to operate microdevices in opaque media in 3D. One promising avenue for future research is the development of polymeric materials that respond to light by mechanically deforming via mechanisms other than photothermal responses. The design of the microdevices will also need improvements as the developed systems move from scientific curiosity to potential technological tools. For instance, light-controlled systems that harness local energy sources will have a clear advantage over light-powered systems, provided that the fuel is compatible with the intended application. It may also be fruitful to consider and integrate different photoresponsive materials and strategies, including light-triggered chemical locomotion and light-controlled mechanical responses, into a single microdevice able to perform a number of tasks with different degrees of autonomy. Key challenges in the field are the movement in complex non-Newtonian fluids, either by individual microrobots or by swarms of micromotors, and the navigation of complex environments by local physical and chemical cues. Advances in reducing power requirements, providing access, and obtaining fast responses and larger forces will be the driver for sophisticated light-based microdevices and their application as microrobots for medical, biological, and microfabrication tasks, as transporters of objects and molecules, and as actuators and active components for larger-scale integrated systems.

Acknowledgements

The authors thank William E. Uspal, Mihail N. Popescu, Alexander von Rohr, Sebastian Trimpe, Hao Zeng, Camilla Parmeggiani, Daniele Martella, and Diederik S. Wiersma for useful discussions on the topics reviewed in this report. The authors also thank Ahmed Mourran for providing Fig. 6(e).

References

[1] A. Ashkin, *Phys. Rev. Lett.* **1970**, *24*, 156.
[2] J. Glückstad, D. Palima, *Light Robotics : Structure-Mediated Nanobiophotonics*, **2017**.
[3] P. -G de Gennes, *Angew. Chemie Int. Ed. English* **1992**, *31*, 842.
[4] A. Walther, A. H. E. Müller, *Chem. Rev.* **2013**, *113*, 5194.
[5] W. F. Paxton, K. C. Kistler, C. C. Olmeda, A. Sen, S. K. St. Angelo, Y. Cao, T. E. Mallouk, P. E. Lammert, V. H. Crespi, *J. Am. Chem. Soc.* **2004**, *126*, 13424.
[6] J. L. Moran, J. D. Posner, *Annu. Rev. Fluid Mech.* **2017**, *49*, 511.
[7] Y. Li, F. Mou, C. Chen, M. You, Y. Yin, L. Xu, J. Guan, *RSC Adv.* **2016**, *6*, 10697.
[8] F. Mou, Y. Li, C. Chen, W. Li, Y. Yin, H. Ma, J. Guan, *Small* **2015**, *11*, 2564.
[9] S. Wang, Z. Jiang, S. Ouyang, Z. Dai, T. Wang, *ACS Appl. Mater. Interfaces* **2017**, *9*, 23974.
[10] H. R. Jiang, N. Yoshinaga, M. Sano, *Phys. Rev. Lett.* **2010**, *105*, 268302.
[11] J. T. Kim, U. Choudhury, H. H. Jeong, P. Fischer, *Adv. Mater.* **2017**, *29*, 1701024.
[12] H. Chen, Q. Zhao, X. Du, *Micromachines* **2018**, *9*, 41.
[13] J. Wang, Z. Xiong, J. Zheng, X. Zhan, J. Tang, *Acc. Chem. Res.* **2018**, *51*, 1957.
[14] L. Xu, F. Mou, H. Gong, M. Luo, J. Guan, *Chem. Soc. Rev.* **2017**, *46*, 6905.
[15] J. Simmchen, J. Katuri, W. E. Uspal, M. N. Popescu, M. Tasinkevych, S. Sánchez, *Nat. Commun.* **2016**, *7*, 10598.
[16] J. Katuri, X. Ma, M. M. Stanton, S. Sánchez, *Acc. Chem. Res.* **2017**, *50*, 2.
[17] S. Sánchez, L. Soler, J. Katuri, *Angew. Chemie Int. Ed.* **2015**, 1414.
[18] S. Sengupta, M. E. Ibele, A. Sen, *Angew. Chemie Int. Ed.* **2012**, *51*, 8434.
[19] K. Hahn, T.-C. Lee, J. G. Gibbs, C. Miksch, M. Alarcón-Correa, P. Fischer, *Nano Lett.* **2014**, *14*, 2407.
[20] M. Safdar, J. Simmchen, J. Jänis, *Environ. Sci. Nano* **2017**, *4*, 1602.
[21] D. P. Singh, U. Choudhury, P. Fischer, A. G. Mark, *Adv. Mater.* **2017**, *29*, 1.
[22] J. Palacci, S. Sacanna, S.-H. Kim, G.-R. Yi, D. J. Pine, P. M. Chaikin, *Philos. Trans. R. Soc. A Math. Phys. Eng. Sci.* **2014**, *372*, 20130372.
[23] J. Palacci, S. Sacanna, A. P. Steinberg, D. J. Pine, P. M. Chaikin, *Science* **2013**, *339*, 936.
[24] J. Palacci, S. Sacanna, A. Vatchinsky, P. M. Chaikin, D. J. Pine, *J. Am. Chem. Soc.* **2013**, *135*, 15978.
[25] B. Dai, J. Wang, Z. Xiong, X. Zhan, W. Dai, C.-C. Li, S.-P. Feng, J. Tang, *Nat. Nanotechnol.* **2016**, *11*, 1087.
[26] Y. Gao, F. Mou, Y. Feng, S. Che, W. Li, L. Xu, J. Guan, *ACS Appl. Mater. Interfaces* **2017**, *9*, 22704.
[27] I. Buttinoni, J. Bialké, F. Kümmel, H. Löwen, C. Bechinger, T. Speck, *Phys. Rev. Lett.* **2013**, *110*, 1.
[28] I. Buttinoni, G. Volpe, F. Kümmel, G. Volpe, C. Bechinger, *J. Phys. Condens. Matter* **2012**, *24*, 284129.
[29] J. Berner, B. Müller, J. R. Gomez-Solano, M. Krüger, C. Bechinger, *Nat. Commun.* **2018**, *9*, 999.
[30] T. Bäuerle, A. Fischer, T. Speck, C. Bechinger, *Nat. Commun.* **2018**, *9*, DOI: 10.1038/s41467-018-05675-7.
[31] B. Liebchen, H. Löwen, *Acc. Chem. Res.* **2018**, *51*, 2982.
[32] F. A. Lavergne, H. Wendehenne, T. Bäuerle, C. Bechinger, *Science* **2019**, *364*, 70.
[33] C. Lozano, B. ten Hagen, H. Löwen, C. Bechinger, *Nat. Commun.* **2016**, *7*, 12828.
[34] R. Dong, Q. Zhang, W. Gao, A. Pei, B. Ren, *ACS Nano* **2016**, *10*, 839.
[35] Q. Zhang, R. Dong, Y. Wu, W. Gao, Z. He, B. Ren, *ACS Appl. Mater. Interfaces* **2017**,

9, 4674.
[36] L. Wang, M. N. Popescu, F. Stavale, A. Ali, T. Gemming, J. Simmchen, *Soft Matter* **2018**, *14*, 6969.
[37] L. Kong, C. C. Mayorga-Martinez, J. Guan, M. Pumera, *ACS Appl. Mater. Interfaces* **2018**, *10*, 22427.
[38] D. Zhou, Y. C. Li, P. Xu, N. S. McCool, L. Li, W. Wang, T. E. Mallouk, *Nanoscale* **2017**, *9*, 75.
[39] R. Dong, Y. Hu, Y. Wu, W. Gao, B. Ren, Q. Wang, Y. Cai, *J. Am. Chem. Soc.* **2017**, *139*, 1722.
[40] B. Jang, A. Hong, H. E. Kang, C. Alcantara, S. Charreyron, F. Mushtaq, E. Pellicer, R. Büchel, J. Sort, S. S. Lee, B. J. Nelson, S. Pané, *ACS Nano* **2017**, *11*, 6146.
[41] J. Zheng, B. Dai, J. Wang, Z. Xiong, Y. Yang, J. Liu, X. Zhan, Z. Wan, J. Tang, *Nat. Commun.* **2017**, *8*, 1438.
[42] É. O'Neel-Judy, D. Nicholls, J. Castañeda, J. G. Gibbs, *Small* **2018**, *14*, 1801860.
[43] C. Chen, S. Tang, H. Teymourian, E. Karshalev, F. Zhang, J. Li, F. Mou, Y. Liang, J. Guan, J. Wang, *Angew. Chemie - Int. Ed.* **2018**, *57*, 8110.
[44] C. Chen, F. Mou, L. Xu, S. Wang, J. Guan, Z. Feng, Q. Wang, L. Kong, W. Li, J. Wang, Q. Zhang, *Adv. Mater.* **2017**, *29*, 1603374.
[45] D. P. Singh, W. E. Uspal, M. N. Popescu, L. G. Wilson, P. Fischer, *Adv. Funct. Mater.* **2018**, *28*, 1706660.
[46] J. J. Abbott, Z. Nagy, F. Beyeler, B. J. Nelson, *Robot. Autom. Mag. IEEE* **2007**, *14*, 92.
[47] B. J. Nelson, I. K. Kaliakatsos, J. J. Abbott, *Annu. Rev. Biomed. Eng.* **2010**, *12*, 55.
[48] J. J. Abbott, O. Ergeneman, M. P. Kummer, A. M. Hirt, B. J. Nelson, *IEEE Trans. Robot.* **2007**, *23*, 1247.
[49] J. J. Abbott, K. E. Peyer, M. C. Lagomarsino, L. Zhang, L. Dong, I. K. Kaliakatsos, B. J. Nelson, *Int. J. Rob. Res.* **2009**, *28*, 1434.
[50] S. Palagi, V. Pensabene, L. Beccai, B. Mazzolai, A. Menciassi, P. Dario, in *Proc. - IEEE Int. Conf. Robot. Autom.*, IEEE, **2011**, pp. 5109–5114.
[51] A. Ghosh, P. Fischer, *Nano Lett.* **2009**, *9*, 2243.
[52] L. Zhang, J. J. Abbott, L. Dong, B. E. Kratochvil, D. Bell, B. J. Nelson, *Appl. Phys. Lett.* **2009**, *94*, 64103.
[53] A. M. Maier, C. Weig, P. Oswald, E. Frey, P. Fischer, T. Liedl, *Nano Lett.* **2016**, *16*, 906.
[54] D. Palima, J. Glückstad, *Laser Photon. Rev.* **2013**, *7*, 478.
[55] M. J. Villangca, D. Palima, A. R. Bañas, J. Glückstad, *Light Sci. Appl.* **2016**, *5*, e16148.
[56] M. Medina-Sánchez, V. Magdanz, M. Guix, V. M. Fomin, O. G. Schmidt, *Adv. Funct. Mater.* **2018**, *28*, 1707228.
[57] G. Lucarini, S. Palagi, L. Beccai, A. Menciassi, *Int. J. Adv. Robot. Syst.* **2014**, *11*, 1.
[58] S. Palagi, B. Mazzolai, C. Innocenti, C. Sangregorio, L. Beccai, *Appl. Phys. Lett.* **2013**, *102*, 124102.
[59] S. Palagi, P. Fischer, *Nat. Rev. Mater.* **2018**, *3*, 113.
[60] W. Hu, G. Z. Lum, M. Mastrangeli, M. Sitti, *Nature* **2018**, *554*, 81.
[61] J. C. Breger, C. Yoon, R. Xiao, H. R. Kwag, M. O. Wang, J. P. Fisher, T. D. Nguyen, D. H. Gracias, *ACS Appl. Mater. Interfaces* **2015**, *7*, 3398.
[62] S. Fusco, H.-W. Huang, K. E. Peyer, C. Peters, M. Häberli, A. Ulbers, A. Spyrogianni, E. Pellicer, J. Sort, S. E. Pratsinis, B. J. Nelson, M. S. Sakar, S. Pané, *ACS Appl. Mater. Interfaces* **2015**, *7*, 6803.
[63] V. Magdanz, G. Stoychev, L. Ionov, S. Sanchez, O. G. Schmidt, *Angew. Chemie - Int. Ed.* **2014**, *53*, 2673.
[64] H.-W. Huang, M. S. Sakar, A. J. Petruska, S. Pané, B. J. Nelson, *Nat. Commun.* **2016**,

7, 12263.
[65] W. Wang, C. Yao, M.-J. Zhang, X.-J. Ju, R. Xie, L.-Y. Chu, *J. Phys. D. Appl. Phys.* **2013**, *46*, 114007.
[66] S. N. Tabatabaei, J. Lapointe, S. Martel, *Adv. Robot.* **2011**, *25*, 1049.
[67] A. Mourran, H. Zhang, R. Vinokur, M. Möller, *Adv. Mater.* **2017**, *29*, 1604825.
[68] H. Zeng, P. Wasylczyk, C. Parmeggiani, D. Martella, M. Burresi, D. S. Wiersma, *Adv. Mater.* **2015**, *27*, 3883.
[69] S. Fusco, M. S. Sakar, S. Kennedy, C. Peters, R. Bottani, F. Starsich, A. Mao, G. A. Sotiriou, S. Pané, S. E. Pratsinis, D. Mooney, B. J. Nelson, *Adv. Mater.* **2014**, 952.
[70] S. Palagi, A. G. Mark, S. Y. Reigh, K. Melde, T. Qiu, H. Zeng, C. Parmeggiani, D. Martella, A. Sanchez-Castillo, N. Kapernaum, F. Giesselmann, D. S. Wiersma, E. Lauga, P. Fischer, *Nat. Mater.* **2016**, *15*, 647.
[71] T. Ding, V. K. Valev, A. R. Salmon, C. J. Forman, S. K. Smoukov, O. A. Scherman, D. Frenkel, J. J. Baumberg, *Proc. Natl. Acad. Sci. U. S. A.* **2016**, *113*, 5503.
[72] A. Gandhi, A. Paul, S. O. Sen, K. K. Sen, *Asian J. Pharm. Sci.* **2015**, *10*, 99.
[73] M. Shibayama, T. Tanaka, in *Responsive Gels Vol. Transitions I*, Springer, Berlin, Heidelberg, **1993**, pp. 1–62.
[74] B. Sierra-Martín, Y. Laporte, A. B. South, L. A. Lyon, A. Fernández-Nieves, *Phys. Rev. E - Stat. Nonlinear, Soft Matter Phys.* **2011**, *84*, 011406.
[75] E. M. Purcell, *Am. J. Phys.* **1977**, *45*, 3.
[76] M. Warner, E. M. Terentjev, *Liquid Crystal Elastomers*, Clarendon Press, **2007**.
[77] M. Camacho-Lopez, H. Finkelmann, P. Palffy-Muhoray, M. Shelley, *Nat. Mater.* **2004**, *3*, 307.
[78] H. Finkelmann, E. Nishikawa, G. G. Pereira, M. Warner, *Phys. Rev. Lett.* **2001**, *87*, 015501.
[79] H. Zeng, D. Martella, P. Wasylczyk, G. Cerretti, J. C. G. Lavocat, C. H. Ho, C. Parmeggiani, D. S. Wiersma, *Adv. Mater.* **2014**, *26*, 2319.
[80] S. Palagi, A. G. Mark, K. Melde, H. Zeng, C. Parmeggiani, D. Martella, D. S. Wiersma, P. Fischer, in *Proc. - Int. Conf. Manip. Autom. Robot. Small Scales, MARSS*, **2016**.
[81] E. Lauga, T. R. Powers, *Reports Prog. Phys.* **2009**, *72*, 96601.
[82] S. Palagi, A. G. Mark, K. Melde, T. Qiu, H. Zeng, C. Parmeggiani, D. Martella, D. S. Wiersma, P. Fischer, in *Proc. - Int. Conf. Manip. Autom. Robot. Small Scales, MARSS*, **2017**.
[83] A. von Rohr, S. Trimpe, A. Marco, P. Fischer, S. Palagi, in *2018 IEEE/RSJ Int. Conf. Intell. Robot. Syst.*, **2018**, pp. 6199–6206.